Heliyon 10 (2024) e25581

Contents lists available at ScienceDirect

Heliyon

journal homepage: www.cell.com/heliyon

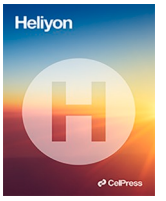

Research article

Green-route synthesis and ab-initio studies of a highly efficient nano photocatalyst:Ce/zinc-oxide nanopetals

Ather Hassan [a,*], Abdul Jalil [a], Syed Zafar Ilyas [a], Muhammad Faisal Iqbal [b], Syed Zulfiqar Ali Shah [a], Yadullah Baqir [c]

[a] Department of Physics, Allama Iqbal Open University, Islamabad, Pakistan
[b] College of Chemistry and Materials Science, Zhejiang Normal University, Jinhua, 321004, China
[c] Department of Agriculture, Allama Iqbal Open University, Islamabad, Pakistan

ARTICLE INFO

Keywords:
Withania coagulans plant
Photodegradation
Ce/zinc-oxide
Density functional theory calculations
Methyl orange

ABSTRACT

In the present work, Zinc-oxide nanostructures and Ce/Zinc-oxide nanopetals were synthesized by a new environmentally friendly green synthesis method using the Withania coagulans plant. Cerium nitrate $Ce(NO_3)_3$ and zinc nitrate $Zn(NO_3)_2$ were used as precursors. The prepared nanostructures were characterized by X-ray diffraction (XRD), scanning electron microscopy (SEM), and ultraviolet spectroscopy (UV–vis). Crystal planes (100), (002), (101), (102), (110), (103), (200), (112) and (201) at 2θ 31.75°, 34.35°, 36.2°, 47.55°, 56.6°, 62.75°, 66.3°, 67.9°, and 69.09° respectively confirmed the hexagonal wurtzite crystal structure of Zinc-oxide. Angular shifts for $Ce_{1\%}$ doped Zinc-oxide and $Ce_{3\%}$ doped Zinc-oxide nanopetal nanostructures were observed in the (100) and (101) planes of the crystal. More specifically, using Scherrer's equation, the crystallite sizes of Zinc-oxide, $Ce_{1\%}$ doped Zinc-oxide nanopetals, $Ce_{3\%}$ doped Zinc-oxide nanopetals, and $Ce_{5\%}$ doped Zinc-oxide nanopetals were 16.48 ± 02 nm, 17.8 ± 2 nm, 18.8 ± 2 nm, and 18.87 ± 2 nm, respectively. The pure Zinc-oxide grain had the appearance of a nanoflower. On the other hand, the nanopetal structure of $Ce_{5\%}$ doped Zinc-oxide nanopetals had oval-shaped nanopetal morphology. The absorption peaks were observed at 373, 376.4, 377, and 378 nm for Zinc-oxide, $Ce_{1\%}$ doped Zinc-oxide nanopetals, $Ce_{3\%}$ doped Zinc-oxide nanopetals, and $Ce_{5\%}$ doped Zinc-oxide nanopetals, respectively, which results in a progressive redshift. The gap energies of Zinc-oxide, $Ce_{1\%}$ doped Zinc-oxide nanopetals, $Ce_{3\%}$ doped Zinc-oxide nanopetals, and $Ce_{5\%}$ doped Zinc-oxide nanopetals were 2.796, 2.645, 2.534, and 2.448 eV, respectively. Photodegradation under visible light (>400 nm) indicates the high efficiency of the photocatalyst based on $Ce_{5\%}$ doped Zinc-oxide nanopetals. DFT calculations, structural changes, charge analysis, and electronic band structures were carried out to confirm the experiment.

1. Introduction

The joint experimental and computational study of Zinc-oxide (ZnO) doped with rare-earth metals has attracted the attention of researchers recently. The interaction of experimental and computational approaches provides a complete understanding of the mechanisms underlying the photocatalytic properties of Zinc-oxide doped with rare-earth metals, which opens the way to the design

* Corresponding author.
E-mail address: ather.hassan@aiou.edu.pk (A. Hassan).

https://doi.org/10.1016/j.heliyon.2024.e25581
Received 28 November 2023; Received in revised form 26 January 2024; Accepted 30 January 2024
Available online 5 February 2024

and development of efficient and stable photocatalytic materials. Experimental studies of Zinc-oxide doped with rare earth metals include the synthesis of material by various methods such as sol-gel, hydrothermal, and chemical precipitation [1].

Density functional theory calculations are used in computational investigations of Zinc-oxide doped with rare earth metals to predict the material's electrical and optical properties [2].

Organic dyes have become an integral part of industries all over the world. Apart from other inorganic pollutants, organic pollutants such as various dyes become part of industrial effluents that affect the life of aquatic organisms. Removal of such pollutants is necessary to preserve the environment. Previously, many researchers and materials engineers have reported efficient composite and doped zinc oxide nanostructures. In this work, cerium-doped zinc oxide nanostructures were synthesized using Withania coagulans plant extract and characterized using experimental and computational tools. In addition, the photocatalytic activity was statistically investigated. Withania coagulans plant has attracted attention in the field of biotechnology and nanotechnology in recent years due to its ability to synthesize nanoparticles. The plant extract has been used as a reducing and capping agent in the synthesis of nanoparticles of various metals and metal oxides and has shown potential for use in various applications such as catalysis, drug delivery, and wastewater treatment [3].

The potential of Zinc-oxide doped with rare earth metals as a photocatalyst has drawn the interest of researchers [4–6]. Compared to pure Zinc-oxide, Zinc-oxide doped with rare earth metals exhibits enhanced photocatalytic activity [7].

Generally, rare earth metals with a narrow band gap absorb light in the visible range, making them suitable for photocatalytic applications. Cerium is a rare earth metal that has been widely studied for its photocatalytic properties. In particular, cerium oxide (CeO_2) has been found to exhibit excellent photocatalytic activity due to its unique electronic and physicochemical properties. One of the key factors behind the photocatalytic activity of cerium oxide is its ability to switch from one oxidation state to another (Ce^{3+} and Ce^{4+}). This property allows cerium oxide to act as a powerful oxidizing agent that promotes various photocatalytic reactions. In addition, cerium oxide has a narrow band gap with an energy of about 3.2 eV [8], which allows it to absorb visible light, making it suitable for photocatalytic applications. The chemical composition of the cerium oxide surface also plays an important role in its photocatalytic activity: the presence of oxygen vacancies and hydroxyl groups on the surface enhances its catalytic properties [9–11].

Zinc-oxide is a versatile material with a wide range of physical, chemical, and optical properties that make it useful in many industrial and technological applications [12]. Zinc-oxide has excellent photocatalytic properties. Zinc-oxide has a broadband gap of about 3.3 eV, which allows it to absorb ultraviolet (UV) radiation, making it an efficient photocatalyst when irradiated with UV light [13]. However, Zinc-oxide also has a number of disadvantages, such as its tendency to photo-corrosion under prolonged UV light irradiation. Strategies to overcome this limitation include doping Zinc-oxide with other materials to improve its stability and durability [14]. Zinc-oxide doped with cerium is a kind of rare-earth metal in which cerium atoms are incorporated into the crystal lattice of Zinc-oxide. This material is widely studied from the point of view of increasing its photocatalytic activity [15–17].

Zong et al. (2014) and Carrillo et al. (2020) observed that Eu-doped Zinc-oxide nanoparticles have a narrower band gap, which facilitates their absorption of visible light and improves their photocatalytic performance [18,19]. Maryam et al. (2022) reported the effect of lanthanide doping on the structural, optical, morphological, antibacterial, and anticancer properties of Zinc-oxide nanoparticles. The results showed that La^{3+}:Zinc-oxide and Ce^{3+}:Zinc-oxide doping formed La_2O_3 and CeO_2 secondary phases, changed the morphology of particles, formed point defects, increased photocatalytic activity, and showed promising anticancer potential [20]. A study by Thi et al. (2017) showed that Lanthanum-doped Zinc-oxide nanostructure can be a promising photocatalyst for visible light photocatalytic applications [21]. Previous studies have reported that pure Zinc-oxide is 71.4 % and Y: Zinc-oxide is 92.3 % efficient in the decomposition of methyl orange [22] and 85 % and 57 % efficient in the decomposition of carbaryl when irradiated with natural sunlight [23]. Similarly, $Zn_{1-2x}Ce_xCe_xYb_xO$ NPs were found to be more efficient photocatalysts for $x = 0.05$ [24,25].

In addition to successful doping, materials scientists have investigated the effect of cerium concentration on the structural properties of Zinc-oxide nanorods (NRs) [26]. They found that increasing the doping cerium concentration leads to an increase in the photoluminescence intensity of cerium-doped Zinc-oxide NRs [27,28]. At the same time, You et al. (2019) confirmed that increasing the concentration of Ce^{3+} ions promotes energy transfer from the host Zinc-oxide to the 5d-energy level of Ce^{3+} ion activators, resulting in increased photoluminescence [29]. The study conducted by S. Karidas et al. (2020) provides important insights into the synthesis and characterization of cerium-doped Zinc-oxide nanoparticles (NPs) and their photocatalytic activity in the degradation of methylene blue [30]. This suggests that cerium-doped Zinc-oxide nanoparticles may be a promising material for environmental applications such as the degradation of pollutants in water [31]. Soren et al. (2015) also suggested that careful control of the doping concentration is important to achieve the desired properties of cerium-doped Zinc-oxide nanoparticles for environmental applications [32]. Manjula et al. (2022) reported the synthesis of CeO_2/Zinc-oxide (CZO) nanostructure resembling microflowers [33]. Using a polymeric templating agent, Yu and H. (2008) and Serrato et al. (2022) demonstrated the highly photocatalytic morphology of CeO_2-Zinc-oxide nanostructure resembling hollow spheres [34,35].

Computational tools such as Density functional theory (DFT) have been carried out to investigate the electronic structure, optical properties and photocatalytic behavior of Zinc-oxide doped with rare earth metals. These computational studies can provide insights into the mechanisms of charge transport, recombination, and capture in doped Zinc-oxide-based photocatalysts and serve as a basis for experiment design and optimization [36]. A study by Feng et al. (2018) showed that the introduction of Cerium into Zinc-oxide significantly changes the optical and electronic properties of Zinc-oxide [37]. Cui et al. (2020) suggested that Sm-doped Zinc-oxide could be a promising material for applications in water splitting and other photocatalytic reactions [38]. Indeed, Feng et al. (2018) showed the potential of Eu-doped Zinc-oxide for various applications beyond photocatalysis. The formation of bound magnetopolarons in Eu-doped Zinc-oxide leads to ferromagnetism [39]. Wen et al. (2018) found that the magnetic behavior of Ce-doped Zinc-oxide crystals changes from ferromagnetic to antiferromagnetic, indicating that the presence of Ce alters the magnetic properties of Zinc-oxide [40].

As Ce concentration increases, Jia et al. (2018) observed that the hybrid conjugation of Ce-4f, Ce-5d, and O-2p states leads to the ferromagnetic behavior of Ce-doped Zinc-oxide [41].

Zhang et al. (2011) used the generalized gradient approximation (GGA) and GGA + U methods in density functional theory calculations to examine the impacts of cerium incorporated in Zinc-oxide. It was discovered that cerium inclusion creates a new localized band between the valence and conduction bands, improving Zinc-oxide's optical properties [42].

2. Experimental section

2.1. Materials and reagent

$Zn(NO_3)_2{\cdot}6H_2O$ (Merck Schuchardt, >99.0 %), $Ce(NO_3)_3{\cdot}6H_2O$ (Merck Schuchardt, >99.0 %) were purchased and used without any further treatment. For oxidation and capping, withania coagulants plant extract was used [3,43–45].

2.2. Synthesis process of Ce-doped zinc-oxide flower-shaped nanopetals

Cerium-doped Zinc-oxide (Ce% doped Zinc-oxide) nanostructures were synthesized using the Withania coagulans plant extract. In order to obtain the plant extract, 10 g of dried leaves of Withania coagulans plant were boiled in 1000 ml distilled water in a glass flask for 2 h. After boiling for 2 h, a light yellow extract was obtained. The extract was further purified by passing through filter paper. In the next step, the $Ce(NO_3)_3{\cdot}6H_2O$ and $Zn(NO_3)_2{\cdot}6H_2O$ were dissolved with the content percentage ratio of 1:99 %, 3:97 %, and 5:95 %, respectively, in the obtained plant solution in three different beakers. To boost the reaction, the obtained solutions in three different beakers were stirred at 80 °C on a hot magnetic plate for 2 h. After 2 h, dark yellow solutions were collected and centrifuged at 3000 rpm for 4 min. The thick slurries of $Ce_{1\%}$ doped Zinc-oxide, $Ce_{3\%}$ doped Zinc-oxide, and $Ce_{5\%}$ doped Zinc-oxide were dried at 80 °C in three different porcelain dishes for 3 h. In order to obtain organic-free nanostructures, the dried samples were heated at 180 °C for 3 h. Pure Zinc-oxide nanostructure was also obtained using the similar method.

2.3. Characterization

The crystallographic structure was investigated using a powder X-ray Diffractometer (D-8 Advance Bruker) equipped with Cu Kα radiation ($\lambda = 0.15406$ nm) source. Morphological analysis was carried out using scanning electron microscopy (SEM, JEOL JSM651). For the assessment of optical bandgap in CuO/Ag nanocomposites, Ultraviolet–visible spectroscopy (UV–Vis, Shimadzu 1700) was used.

The photocatalytic activity of Zinc-oxide and Ce-doped Zinc-oxide photocatalysts was tested by the degradation of methyl orange (MO) as a model pollutant under visible light with a wavelength greater than 400 nm. Methyl orange is a commonly used organic dye that is often employed as a model pollutant in photocatalytic studies due to its well-defined absorbance spectra and high sensitivity to photocatalytic degradation.

Density Functional calculations were executed through the plane-wave pseudopotential method [46,47]. The generalized gradient approximation (GGA) was used to depict the exchange-correlation potential in the Perdew-Burke-Ernzerh (PBE) form [48–50]. To achieve optimal outcomes and prevent electron leakage, the RMT × Kmax = 8.00 basis functions and 25000 k points were used. In the Monkhorst-Pack approach, the Brillouin zone was discretized using 4 × 4 × 2 k-point meshes. Furthermore, the cut-off energy of the plane wave for the equipotential muffin tin sphere can be set at 380 eV. This results in the materials' most stable structural features. The following convergence tolerances are established during geometry optimization: The convergence energy is 2.0×10^{-5} eV atom-1; the maximum strength is 0.05 eV $Å^{-1}$; the maximum stress on each cell is 0.1 GPa; the maximum offset of each atom is 0.002 Å and the self-consistent field (SCF) is set to 2.0×10^{-6} eV $atom^{-1}$.

2.4. Photocatalysis

A photocatalytic process is a process that uses light energy to trigger a chemical reaction on a surface. In a photocatalytic reaction, a substance called a photocatalyst is used to absorb light energy and initiate or accelerate the chemical reaction. The photocatalyst is usually a semiconductor material, such as Zinc-oxide (ZnO), which can generate electron-hole pairs when light is absorbed.

The electron-hole pairs generated in the photocatalyst can react with molecules adsorbed on or near its surface to form highly reactive intermediates that can trigger chemical reactions. These reactions can be used to break down pollutants such as volatile organic compounds, nitrogen oxides, and other organic molecules into harmless substances [51]. Cerium-doped zinc-oxide is a type of photocatalyst used in photocatalysis to break down pollutants in water. The addition of cerium to zinc-oxide can improve its photocatalytic properties by increasing its light absorption and ability to separate charges.

Photocatalytic activity can be assessed by measuring the degradation rate of target contaminants when irradiated with ultraviolet or visible light. The most commonly used contaminants are organic dyes such as methylene blue (MB), which can be easily monitored by UV–Vis spectroscopy.

3. Results and discussion

The dimensions and shape of the materials can have significant effects on their properties. A scanning electron microscope was used

to analyze morphology (Fig. 1). The surface morphology of pure Zinc-oxide (Fig. 1 a, b) and $Ce_{5\%}$ doped Zinc-oxide nanopetals (Fig. 1 c, d) is homogeneous and smooth, according to the SEM images. Pure Zinc-oxide displayed nanopetals in the form of nanoflowers. Based on earlier studies documented in the literature, the diameter of the nanopetals is around several nanometers [52]. Zinc-oxide is known to have a high surface area due to its nanoflower-like form, which is helpful for photocatalysis. On the other hand, $Ce_{5\%}$ doped Zinc-oxide has oval-shaped nanoflower-like nanopetals, which suggests that their surface area is greater than that of pure Zinc-oxide. Ce-doped Zinc-oxide's greater surface area may lessen charge recombination, which could result in effective pollutant photodegradation.

Using an X-ray diffractometer, structural analysis was performed on flower-shaped nanopetals of Zinc-oxide, $Ce_{1\%}$ doped Zinc-oxide, $Ce_{3\%}$ doped Zinc-oxide, and $Ce_{5\%}$ doped Zinc-oxide in the 2θ range of 20–80°. Fig. 2 a exposes the (100), (002), (101), (102), (110), (103), (200), (112) and (201) planes of the flower-shaped nanopetals of Zinc-oxide that exhibit sharp peaks at 2θ 31.75°, 34.35°, 36.2°, 47.55°, 56.6°, 62.75°, 66.3°, 67.9°, and 69.09° respectively, as revealed by the XRD spectrum. The hexagonal wurtzite crystal structure of Zinc-oxide and the Joint Committee Powder Diffraction Standards (JCPDS number 36–1451) fit the observed peaks and their matching planes quite well [53,54]. The impact of cerium doping was examined using the XRD spectrum; a magnified XRD pattern is shown in Fig. 2b. Because of the Ce inclusion in the structure, peak shifting of the 1 % and 3 % Ce/Zinc-oxide nanopetals nanostructures was seen at the planes of (100) and (101). Ce^{3+} and Ce^{4+} have greater ionic radii (1.03 Å > 0.97 Å > 0.74 Å) than Zn^{2+}. However, there is no corresponding increase in lattice parameters for higher doping of Ce contents (5 %), which indicates some defects and compensates the increasing ionic radii. Furthermore, samples with a Ce content ranging from 1 to 5 % doping of cerium showed a decrease in the width of the diffraction peaks. The X-ray spectra of the 1 %, 3 %, and 5 % Ce/Zinc-oxide nanopetals demonstrated the successful synthesis of a nanostructure. The Scherrer equation was utilized to compute the sizes of the crystallites. The measured diameters of the crystallites were determined to be 16.48 ± 02 nm for pure Zinc-oxide and 17.8 ± 2, 18.8 ± 2, and 18.87 ± 2 nm for nanopetals containing 1 %, 3 %, and 5 % of Ce/Zinc-oxide, respectively. The crystal size of produced Ce/Zinc-oxide nanocomposites was estimated to be in the range of 16.48–18.87 nm in a previous study applying the Scherrer equation. The Ostwald ripening phenomena suggests that relatively large particles growing at the expense of smaller ones may be the cause of the 3 % doping of Ce ions and subsequent rise in crystallite size [55]. Wegard's law states that the lattice parameters rise according to the Ce3+ concentration [56]. The full-width half-maximum (FWHM) was determined following a peak fitting (Fig. 2 c). For pure Zinc-oxide, $Ce_{1\%}$ doped Zinc-oxide, $Ce_{3\%}$ doped Zinc-oxide, and $Ce_{5\%}$ doped Zinc-oxide nanopetals, the estimated FWHM values were computed as 0.51, 0.45, 0.42, and 0.41, respectively. The breadth of the diffraction peaks, or the drop in FWHM, appears to diminish when Ce concentration rises from 1 to 5 wt percent. This suggests that the crystalline nature and properties of the Ce-doped Zinc-oxide samples are enhanced.

The bandgap energies of the pure Zinc-oxide and Ce/Zinc-oxide nanopetals were significantly different, according to UV–Vis spectroscopy. Zinc-oxide, $Ce_{1\%}$ doped Zinc-oxide nanopetals, $Ce_{3\%}$ doped Zinc-oxide nanopetals, and $Ce_{5\%}$ doped Zinc-oxide nanopetals all showed absorption maxima at 373, 376.4, 377, and 378 nm, respectively. The redshift happens and advances toward higher wavelengths, as shown by the UV–Vis spectrum (Fig. 3 a). Ce3+ ions' tendency to re-absorb light may be the cause of the redshift seen in Ce/Zinc-oxide nanopetals [57]. The energy gaps of the synthesized materials were calculated from the Tac plot and measured were found as 2.796, 2.645, 2.534, and 2.448 eV for the pure Zinc-oxide, $Ce_{1\%}$ doped Zinc-oxide, $Ce_{3\%}$ doped Zinc-oxide, and $Ce_{5\%}$ doped Zinc-oxide nanopetals, respectively (Fig. 3 b). The doping of cerium atoms caused the change in the energy band gap, which may

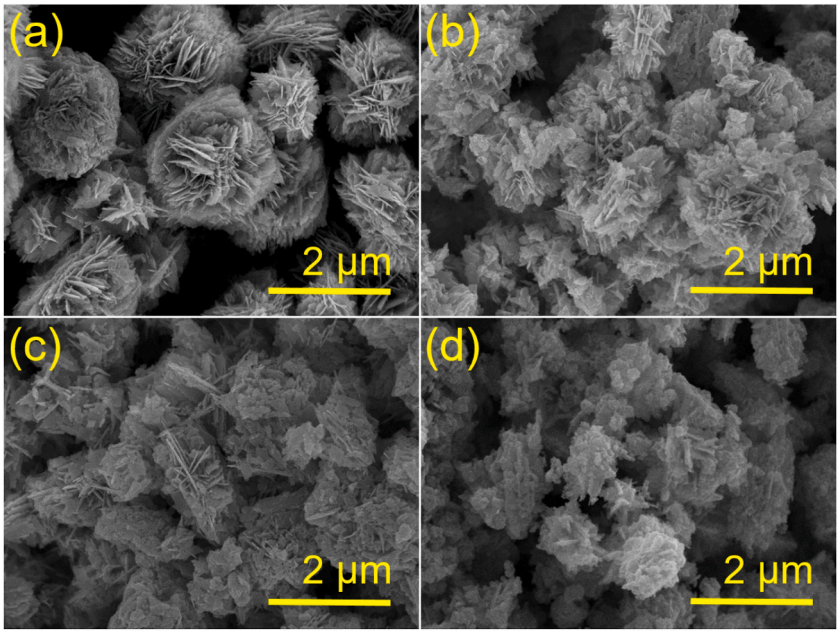

Fig. 1. SEM images of (a, b) Zinc-oxide and (c, d) $Ce_{5\%}$ doped Zinc-oxide flower-shaped nanopetals.

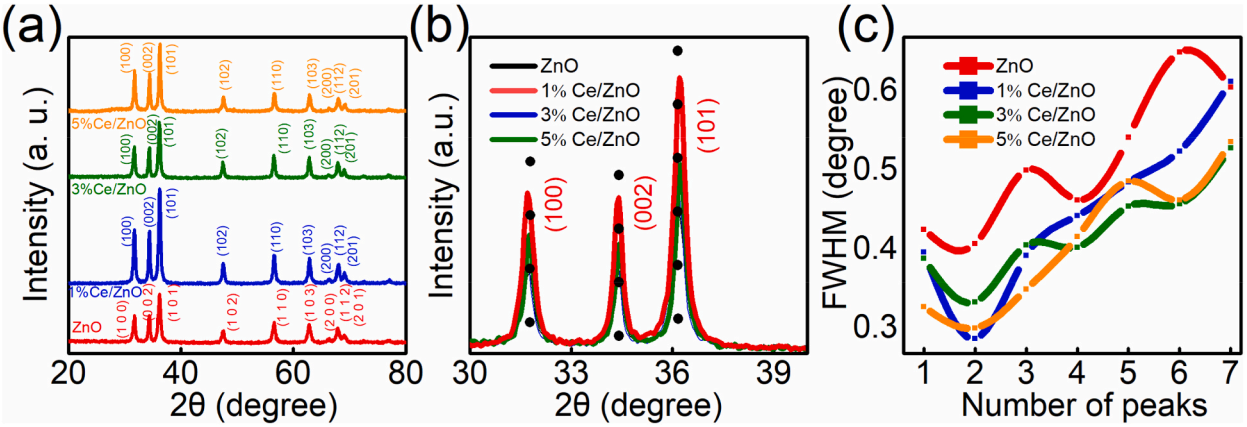

Fig. 2. (a) XRD pattern (b) Zoomed major peaks of different planes (c) Full-width half-maximum (FWHM).

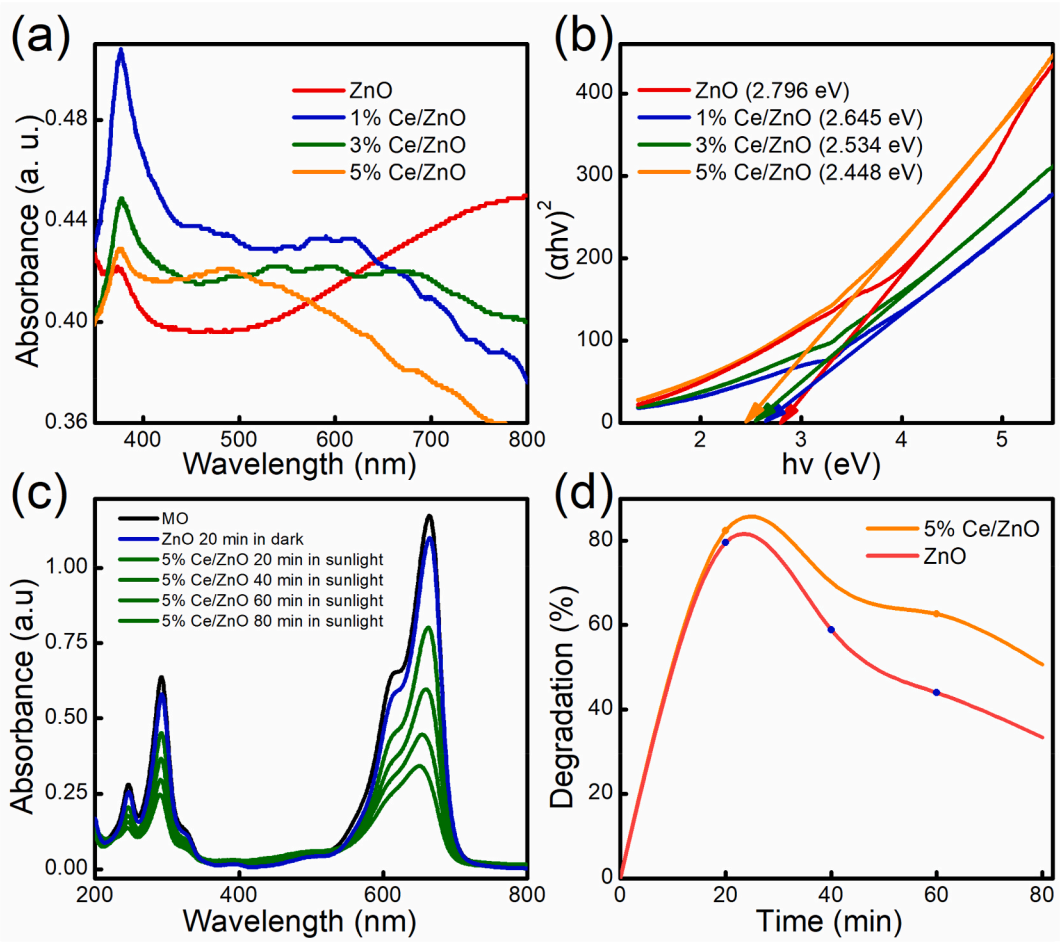

Fig. 3. (a) Absorption spectra of Zinc-oxide, $Ce_{1\%}$ doped Zinc-oxide, $Ce_{3\%}$ doped Zinc-oxide and $Ce_{5\%}$ doped Zinc-oxide (b) $(\alpha h\nu)^2$ with $h\nu$ for the Zinc-oxide and Ce-doped Zinc-oxide (c) Absorption spectra demonstrating the photocatalytic degradation of MO solution in the presence of Zinc-oxide, and $Ce_{5\%}$ doped Zinc-oxide (d) Percent degradation of MO.

produce the photoelectronic trapping centers during the photocatalysis process. Based on the Tac plot, the energy gaps of the produced materials were determined to be 2.796, 2.645, 2.534, and 2.448 eV for the nanopetals of pure Zinc-oxide, 1 %, 3 %, and 5 % Ce/Zinc-oxide, respectively (Fig. 3b). The energy band gap changed as a result of the doping of cerium atoms, and this could lead to the

production of photoelectronic trapping centers during photocatalysis. The emergence of new energy states in the band gap that capture photoelectrons and cause a drop in energy band gap values at greater doping concentrations is what causes the change in the energy band gap. The redshift of the absorption edges in Ce-doped Zinc-oxide photocatalysts was also reported by Liu et al. [58]. The introduction of defects within the crystal by dopants has the potential to greatly improve the photocatalytic activity of doped Zinc-oxide nanocatalysts [59].

The observed redshift is caused by charge transfer transitions between the valence band/conduction band (CB/VB) of Zinc-oxide and the lanthanide 'f' electrons. Ce^{3+} ions interact with the Zinc-oxide CB/VB through partially filled 4f orbitals, which results in the observed alterations in the absorption spectra. The absorption spectra show a redshift in the band gap from 2.796 eV to 2.448 eV, which suggests that Ce^{3+} ions have added more energy levels to Zinc-oxide's band gap. This has the effect of decreasing the energy needed for light absorption [60]. This redshift may have a significant impact on the material's optical and electrical characteristics since it may change how the material behaves in situations where light absorption and emission are critical, such as optoelectronic devices, photocatalysis, and sensors.

Significant details on the photocatalytic activity of the materials are revealed by the absorption spectra of methylene orange (MO) degradation on Zinc-oxide and Zinc-oxide doped with Ce ions under visible light irradiation (Fig. 3 c).

The findings show that $Ce_{5\%}$ doped Zinc-oxide demonstrated strong photocatalytic activity, degrading most of the methylene orange in less than 100 min, including dark time (Fig. 3 d). This implies that under visible light irradiation, the $Ce_{5\%}$ doped Zinc-oxide photocatalyst is quite effective in breaking down methylene orange.

The two samples' Zinc-oxide and $Ce_{5\%}$ doped Zinc-oxide nanopetals' MO degradation data are statistically analyzed (Fig. 4). A linear regression analysis of the degradation data was done in order to determine the correlation coefficient (R^2) between the time and the MO's degradation and to construct a model that represented the degradation.

For Zinc-oxide photocatalyst, degradation follows a polynomial of order 2 ($y = at^2 - bt^1 + c$), but for Ce/Zinc-oxide nanopetals photocatalyst, degradation follows a linear equation ($y = at + b$). where t is the time in minutes and a, b, and c are constants. Zinc-oxide and $Ce_{5\%}$ doped Zinc-oxide nanopetals were found to have correlation coefficients (R^2) of 0.9999 and 0.9924, respectively. Piecewise linear regression splitting is used to optimize the degradation model for the samples (Zinc-oxide and Ce-doped Zinc-oxide nanopetals), resulting in two segments that have improved correlation coefficients (R^2).

The findings imply that the dopant presence of Ce ions in Zinc-oxide can greatly increase Zinc-oxide's visible light photocatalytic activity, which will result in a more effective breakdown of methylene orange. The photocatalytic performance of Zinc-oxide appears to be positively impacted by the specific concentration of Ce ions (in this example, 5 %), leading to a faster breakdown of methylene orange in a comparatively short amount of time—100 min.

These results demonstrate the efficacious photocatalytic degradation of organic pollutants, like methylene orange, by Ce-doped Zinc-oxide photocatalysts, especially the $Ce_{5\%}$ doped Zinc-oxide. They also point to the possibility of using these catalysts in environmental remediation and pollution control applications.

The $P6_3mc$, C6v-4 symmetry Zinc-oxide hexagonal wurtzite model is the ideal structure that was employed in the investigation [61]. The simulated XRD, as shown in Fig. 5c–is consistent with earlier research. The initial lattice parameters are: $a = b = 3.249$ Å, $c = 5.206$ Å, $\alpha = \beta = 90^\circ$ and $\gamma = 120^\circ$ [62]. The optimized supercell models for pure and Ce-doped Zinc-oxide are displayed in Fig. 5a and b. To create $Zn_{0.9}Ce_{0.1}O$, Ce atoms are substituted for Zn atoms in accordance with the Zinc-oxide model.

As illustrated in Fig. 5f, it was found that the bond length and bond angles of Zinc-oxide are, respectively, 1.994 Å and $\alpha = \beta = 110.21^\circ$ and $\gamma = 108.71^\circ$. However, as can be shown in Fig. 5g, the bond lengths and bond angles of Ce-doped Zinc-oxide are 2.219, 2.185, and 2.179 Å, and $\alpha = \beta = 107.81^\circ$ and $\gamma = 107.69^\circ$, separately.

These findings are in agreement with the experimental data and imply that the insertion of Ce ions into the Zinc-oxide lattice results

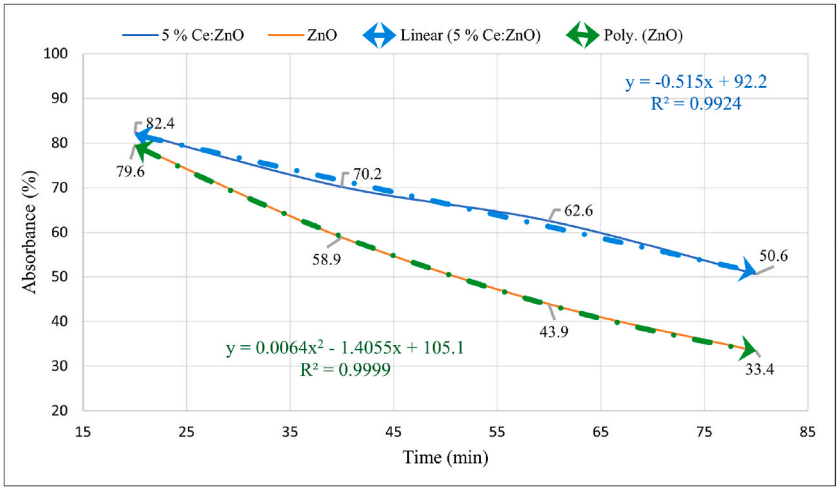

Fig. 4. Mo degradation with interpolation.

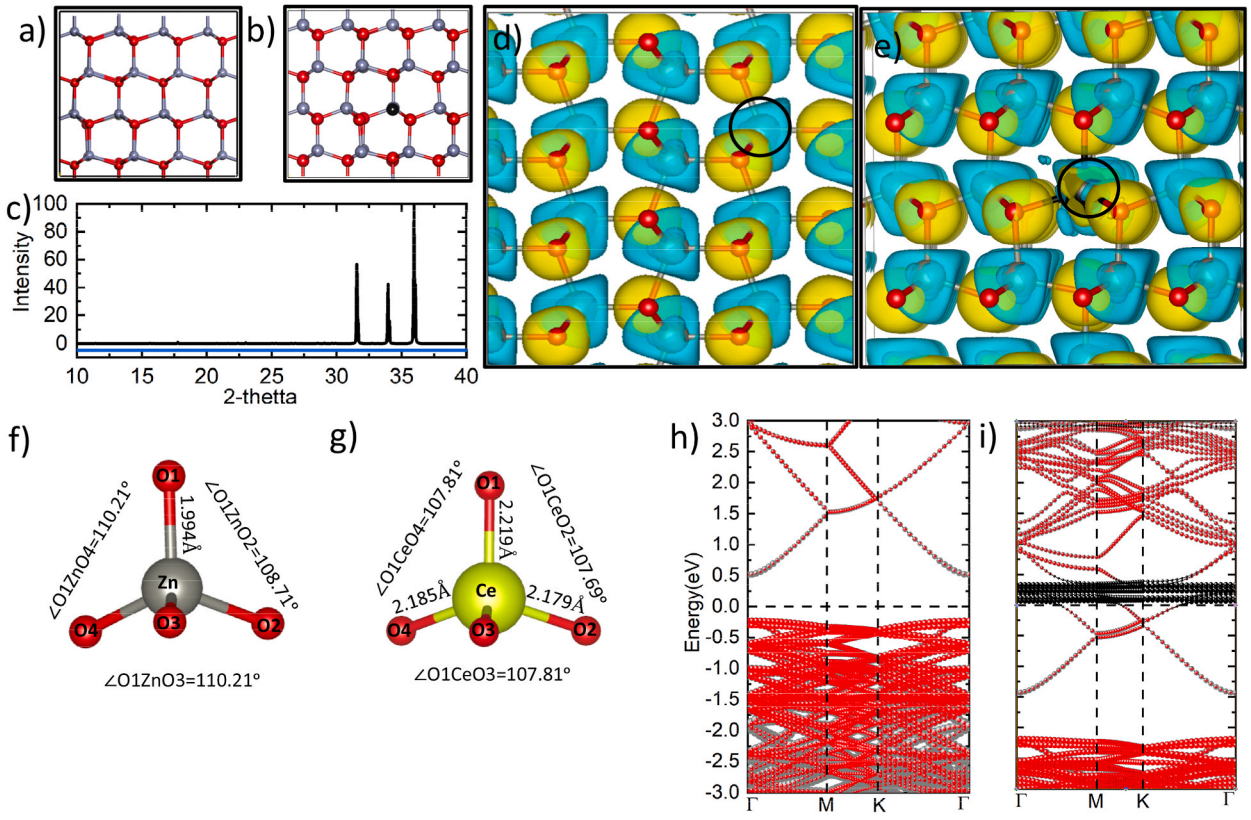

Fig. 5. (a) Crystal structure of Zinc-oxide (b) Crystal structure of Ce/Zinc-oxide nanopetals (c) Simulated XRD of Ce/Zinc-oxide nanopetals (d) & (e) Differential charge density of t and Ce/Zinc-oxide nanopetals (f) & (g) bond lengths and bond angles of Zinc-oxide and Ce/Zinc-oxide nanopetals (h) & (i) Band structures of Zinc-oxide and Ce/Zinc-oxide nanopetals.

in a little structural distortion. One Zn atom was substituted with a Ce atom in a 4 × 2 × 2 supercell of relaxed Zinc-oxide, increasing the bond length from 1.994 to 2.194 Å.

Additionally, as illustrated in Fig. 5d & e, the Zincoxide's differential charge density and the differential charge density of the cerium-doped zinc-oxide nanostructure are computed.

Based on the baders charge analysis, the Cerium atom transfers ~0.93e to O atoms in the Zinc-oxide structure, as shown in Fig. 5d. (The yellow color shows depletion and the green represents the buildup of charges). Fig. 5e illustrates how the net charge transfers to the O atom in Cerium-doped Zinc-oxide are around 0.911e. As seen in Fig. 5h & i, the band structures of Zinc-oxide and Cerium-doped Zinc-oxide are plotted to observe the electronic change in structure. Pure Zinc-oxide's band gap is 0.7 eV, following earlier DFT predictions [63]. Cerium-doped Zinc-oxide now has a smaller band gap, which is in line with the results of the experiment. The formation energies for Ce/Zinc-oxide nanopetals and pure Zinc-oxide nanopetals nanostructures were −3.924 eV/atom and −4.328 eV/atom, respectively. This validates the stable structures' thermodynamic advantage.

4. Conclusions

A novel green route method using an organic extract of the *Withania coagulans* plant was effectively exploited in Ce/Zinc-oxide nanopetals synthesis. The X-ray diffractograms of the Zinc-oxide, $Ce_{1\%}$ doped Zinc-oxide nanopetals, $Ce_{3\%}$ doped Zinc-oxide nanopetals and $Ce_{5\%}$ doped Zinc-oxide nanopetals showed sharp peaks that correspond to the crystal planes (100), (002), (101), (102), (110), (103), (200),(112), and (201) of the hexagonal wurtzite crystal structure of Zinc-oxide. The particles of the fabricated structure had a nanoflower-like morphology consisting of nanosheets about 1–2 nm in diameter. A crystallite size of about 18 nm was determined. In contrast, $Ce_{5\%}$ doped Zinc-oxide nanopetals exhibited oval-shaped nanoflowers-like morphology, indicating a larger surface area compared to pure Zinc-oxide. Zinc-oxide and Ce/Zinc-oxide nanopetals nanostructures have significantly different bandgap energies, as revealed by UV–Vis spectroscopy. The energy gaps of 2.796, 2.645, 2.534, and 2.448 eV were observed for Zinc-oxide, $Ce_{1\%}$ doped Zinc-oxide nanopetals, $Ce_{3\%}$ doped Zinc-oxide nanopetals, and $Ce_{5\%}$ doped Zinc-oxide nanopetals respectively. DFT analysis is used to evaluate the bandgap's decreasing tendency. The photocatalytic activity was analyzed statistically. Degradation followed the polynomial of order 2 ($y = at^2 - bt^1 + c$) for Zinc-oxide photocatalyst and linear equation ($y = at + b$) for Ce/Zinc-oxide nanopetals photocatalyst. The findings suggested that the particular concentration of Ce ions—in this case, 5%—seems to have a positive impact on Zinc-oxide's photocatalytic activity, leading to a faster pace of methylene orange breakdown.

Data availability statement

All the data are available in this manuscript, and the related data can be available from the corresponding author.

CRediT authorship contribution statement

Ather Hassan: Writing – original draft. **Abdul Jalil:** Writing – review & editing. **Syed Zafar Ilyas:** Conceptualization. **Muhammad Faisal Iqbal:** Methodology. **Syed Zulfiqar Ali Shah:** Formal analysis. **Yadullah Baqir:** Software, Formal analysis.

Declaration of competing interest

The authors declare that they have no known competing financial interests or personal relationships that could have appeared to influence the work reported in this paper.

Acknowledgments

We acknowledge the guidance and support of Professor Dr. Simeon Agathopoulos

References

[1] F. Sanakousar, et al., Recent progress on visible-light-driven metal and non-metal doped ZnO nanostructures for photocatalytic degradation of organic pollutants, Mater. Sci. Semicond. Process. 140 (2022) 106390.
[2] A. El Hachimi, et al., First-principles prediction of the magnetism of 4f rare-earth-metal-doped wurtzite zinc oxide, J. Rare Earths 32 (8) (2014) 715–721.
[3] D. Tripathi, et al., Green and cost effective synthesis of silver nanoparticles from endangered medicinal plant Withania coagulans and their potential biomedical properties, Mater. Sci. Eng. C 100 (2019) 152–164.
[4] W. Raza, D. Bahnemann, M. Muneer, A green approach for degradation of organic pollutants using rare earth metal doped bismuth oxide, Catal. Today 300 (2018) 89–98.
[5] P. Singh, R.K. Singh, R. Kumar, Journey of ZnO quantum dots from undoped to rare-earth and transition metal-doped and their applications, RSC Adv. 11 (4) (2021) 2512–2545.
[6] P. Pascariu, et al., Novel rare earth (RE-La, Er, Sm) metal doped ZnO photocatalysts for degradation of Congo-Red dye: synthesis, characterization and kinetic studies, J. Environ. Manag. 239 (2019) 225–234.
[7] M. Faisal, et al., Highly efficient photocatalyst based on Ce doped ZnO nanorods: controllable synthesis and enhanced photocatalytic activity, Chem. Eng. J. 229 (2013) 225–233.
[8] A.S. Thill, et al., Shifting the band gap from UV to visible region in cerium oxide nanoparticles, Appl. Surf. Sci. 528 (2020) 146860.
[9] S. Yabe, T. Sato, Cerium oxide for sunscreen cosmetics, J. Solid State Chem. 171 (1–2) (2003) 7–11.
[10] S. Sumathi, A. Kavipriya, Structural, optical and photocatalytic activity of cerium doped zinc aluminate, Solid State Sci. 65 (2017) 52–60.
[11] Z. Kalaycıoğlu, B. Geçim, F.B. Erim, Green synthesis of cerium oxide nanoparticles from turmeric and kinds of honey: characterisations, antioxidant and photocatalytic dye degradation activities, Adv. Nat. Sci. Nanosci. Nanotechnol. 13 (1) (2022) 015016.
[12] M. Garcia, et al., Magnetic properties of ZnO nanoparticles, Nano Lett. 7 (6) (2007) 1489–1494.
[13] A. Chauhan, et al., Photocatalytic dye degradation and antimicrobial activities of Pure and Ag-doped ZnO using Cannabis sativa leaf extract, Sci. Rep. 10 (1) (2020) 7881.
[14] T. Khalafi, F. Buazar, K. Ghanemi, Phycosynthesis and enhanced photocatalytic activity of zinc oxide nanoparticles toward organosulfur pollutants, Sci. Rep. 9 (1) (2019) 1–10.
[15] L. Wang, et al., Preparation and optical and photocatalytic properties of Ce-doped ZnO microstructures by simple solution method, Mater. Sci. Semicond. Process. 71 (2017) 401–408.
[16] P. Boontueng, et al., Synthesis and characterization of Ce3+-doped barium-gadolinium-fluoroborate glasses for proton beam diagnostic, Optik 287 (2023) 171134.
[17] N. Aisah, et al., Synthesis and enhanced photocatalytic activity of Ce-doped zinc oxide nanorods by hydrothermal method, in: IOP Conference Series: Materials Science and Engineering, IOP Publishing, 2017.
[18] Y. Zong, et al., Synthesis and high photocatalytic activity of Eu-doped ZnO nanoparticles, Ceram. Int. 40 (7) (2014) 10375–10382. Part B).
[19] M.A. Hernández-Carrillo, et al., Eu-modified ZnO nanoparticles for applications in photocatalysis, Catal. Today 349 (2020) 191–197.
[20] M. Al Bitar, et al., Characterization and evaluation of the therapeutic benefits of pure and lanthanides mono- and co-doped zinc oxide nanoparticles, Saudi J. Biol. Sci. 30 (4) (2023) 103608.
[21] V.H.-T. Thi, B.-K. Lee, Effective photocatalytic degradation of paracetamol using La-doped ZnO photocatalyst under visible light irradiation, Mater. Res. Bull. 96 (2017) 171–182.
[22] I. Massoudi, et al., Effect of yttrium substitution on microstructural, optical, and photocatalytic properties of ZnO nanostructures, J. Electron. Mater. 49 (9) (2020) 5353–5362.
[23] S. Sujinnapram, S. Wongrerkdee, Synergistic effects of structural, crystalline, and chemical defects on the photocatalytic performance of Y-doped ZnO for carbaryl degradation, J. Environ. Sci. 124 (2023) 667–677.
[24] E. Hannachi, et al., Synthesis, characterization, and evaluation of the photocatalytic properties of zinc oxide co-doped with lanthanides elements, J. Phys. Chem. Solid. 170 (2022) 110910.
[25] P. Chand Sukriti, V. Singh, Enhanced visible-light photocatalytic activity of samarium-doped zinc oxide nanostructures, J. Rare Earths 38 (1) (2020) 29–38.
[26] M. Carofiglio, et al., Doped zinc oxide nanoparticles: synthesis, characterization and potential use in nanomedicine, Appl. Sci. 10 (15) (2020) 5194.
[27] J.L. Cervantes-López, et al., Photoluminescence on cerium-doped ZnO nanorods produced under sequential atomic layer deposition–hydrothermal processes, Appl. Phys. A 123 (1) (2016) 86.
[28] B. Abderrahmane, et al., Improvement of ZnO nanorods photoelectrochemical, optical, structural and morphological characterizations by cerium ions doping, J. Alloys Compd. 829 (2020) 154498.
[29] S. You, et al., Tuning ZnO nanorods photoluminescence through atmospheric plasma treatments, Apl. Mater. 7 (8) (2019) 081111.
[30] S. Karidas, et al., Photodegradation of methylene blue (MB) using cerium-doped zinc oxide nanoparticles, Sādhanā 45 (1) (2020) 128.
[31] G. Flores-Carrasco, et al., ZnO nanoparticles with controllable Ce content for efficient photocatalytic degradation of MB synthesized by the polyol method, Catalysts 11 (2021), https://doi.org/10.3390/catal11010071.
[32] S. Soren, M. Bessoi, P. Parhi, A rapid microwave initiated polyol synthesis of cerium oxide nanoparticle using different cerium precursors, Ceram. Int. 41 (6) (2015) 8114–8118.

[33] M. Natesan, et al., Ceria-doped zinc oxide nanorods assembled into microflower architectures as electrocatalysts for sensing of piroxicam in urine sample, Colloids Surf. A Physicochem. Eng. Asp. 642 (2022) 128697.
[34] J. Yu, X. Yu, Hydrothermal synthesis and photocatalytic activity of zinc oxide hollow spheres, Environ. Sci. Technol. 42 (13) (2008) 4902–4907.
[35] E. Cerrato, et al., Zinc oxide hollow spheres decorated with cerium dioxide. The role of morphology in the photoactivity of semiconducting oxides, J. Phys. Condens. Matter 34 (13) (2022) 134001.
[36] M. Khuili, et al., First-principles calculations of rare earth (RE=Tm, Yb, Ce) doped ZnO: structural, optoelectronic, magnetic, and electrical properties, Vacuum 181 (2020) 109603.
[37] Y. Feng, et al., A first-principle study on photoelectric characteristics of Ce-doped ZnO, Ferroelectrics 573 (1) (2021) 214–223.
[38] Q. Wu, et al., First-Principles calculations of the electronic structure and optical properties of yttrium-doped ZnO monolayer with vacancy, Materials 13 (3) (2020) 724.
[39] Q. Ling-Feng, et al., Effects of Eu doping and O vacancy on the magnetic and optical properties of ZnO, Phys. B Condens. Matter 530 (2018) 133–141.
[40] J.-Q. Wen, et al., The investigation of Ce doped ZnO crystal: the electronic, optical and magnetic properties, Phys. B Condens. Matter 534 (2018) 44–50.
[41] X.F. Jia, et al., Effect of Ce doping on the magnetic and optical properties of ZnO by the first principle, J. Magn. Magn Mater. 465 (2018) 128–135.
[42] Y.-H. Zhang, et al., A room-temperature aniline sensor based on Ce doped ZnO porous nanosheets with abundant oxygen vacancies, J. Alloys Compd. 885 (2021) 160988.
[43] R. Maurya, Chemistry and pharmacology of Withania coagulans: an Ayurvedic remedy, J. Pharm. Pharmacol. 62 (2) (2010) 153–160.
[44] R. Jain, S. Kachhwaha, S. Kothari, Phytochemistry, pharmacology, and biotechnology of Withania somnifera and Withania coagulans: a review, J. Med. Plants Res. 6 (41) (2012) 5388–5399.
[45] V. Gupta, B.B. Keshari, Withania coagulans Dunal (paneer doda): a review, International Journal of Ayurvedic and Herbal Medicine 3 (5) (2013) 1330–1336.
[46] H.E. Krizner, D.O. De Haan, J. Kua, Thermodynamics and kinetics of methylglyoxal dimer formation: a computational study, J. Phys. Chem. 113 (25) (2009) 6994–7001.
[47] M.C. Payne, et al., Iterative minimization techniques for ab initio total-energy calculations: molecular dynamics and conjugate gradients, Rev. Mod. Phys. 64 (4) (1992) 1045.
[48] J.P. Perdew, K. Burke, M. Ernzerhof, Generalized gradient approximation made simple, Phys. Rev. Lett. 77 (18) (1996) 3865.
[49] X. Chen, et al., First-principles study of the effect of functional groups on polyaniline backbone, Sci. Rep. 5 (1) (2015) 16907.
[50] X. Chen, et al., Functionalization-induced changes in the structural and physical properties of amorphous polyaniline: a first-principles and molecular dynamics study, Sci. Rep. 6 (1) (2016) 20621.
[51] K. Anandan, V. Rajendran, Effects of Mn on the magnetic and optical properties and photocatalytic activities of NiO nanoparticles synthesized via the simple precipitation process, Mater. Sci. Eng., B 199 (2015) 48–56.
[52] H. Parangusan, et al., Nanoflower-like yttrium-doped ZnO photocatalyst for the degradation of methylene blue dye, Photochem. Photobiol. 94 (2) (2018) 237–246.
[53] A. George, et al., Detailed of X-ray diffraction and photoluminescence studies of Ce doped ZnO nanocrystals, J. Alloys Compd. 509 (20) (2011) 5942–5946.
[54] N.K. Rajendran, et al., Synthesis of zinc oxide nanoparticles using Rubus fairholmianus root extract and their activity against pathogenic bacteria, Molecules 26 (10) (2021) 3029.
[55] S. Suwanboon, et al., Optical and photocatalytic properties of La-doped ZnO nanoparticles prepared via precipitation and mechanical milling method, Ceram. Int. 39 (3) (2013) 2811–2819.
[56] H.-L. Shi, Y. Duan, Band-gap bowing and p-type doping of (Zn, Mg, Be) O wide-gap semiconductor alloys: a first-principles study, Eur. Phys. J. B 66 (2008) 439–444.
[57] H. Xu, et al., Enhanced photocatalytic activity of Ag3VO4 loaded with rare-earth elements under visible-light irradiation, Ind. Eng. Chem. Res. 48 (24) (2009) 10771–10778.
[58] I.-T. Liu, M.-H. Hon, L.G. Teoh, The preparation, characterization and photocatalytic activity of radical-shaped CeO2/ZnO microstructures, Ceram. Int. 40 (3) (2014) 4019–4024.
[59] I. Ahmad, et al., ZnO and Ni-doped ZnO photocatalysts: synthesis, characterization and improved visible light driven photocatalytic degradation of methylene blue, Inorg. Chim. Acta. 543 (2022) 121167.
[60] Sukriti, et al., Rapid visible light-driven photocatalytic degradation using Ce-doped ZnO nanocatalysts, Vacuum 178 (2020) 109364.
[61] F.-w. Xie, et al., First-principle study of optical properties of (N, Ga) codoped ZnO, Opt Commun. 285 (10–11) (2012) 2660–2664.
[62] Y. Park, et al., First-principles studies of the electronic and dielectric properties of Si/SiO2/HfO2 interfaces, Jpn. J. Appl. Phys. 52 (4R) (2013) 041803.
[63] Z. Ma, et al., Cu-doped ZnO electronic structure and optical properties studied by first-principles calculations and experiments, Materials 12 (1) (2019) 196.